ELSEVIER

Composites: Part A 32 (2001) 207–220

composites
Part A: applied science and manufacturing

www.elsevier.com/locate/compositesa

Numerical simulation of injection/compression liquid composite molding. Part 2: preform compression

K.M. Pillai[a,1], C.L. Tucker[a,*], F.R. Phelan[b]

[a]*Department of Mechanical and Industrial Engineering, University of Illinois, 1206 W. Green St., Urbana, IL 61801, USA*
[b]*Polymer Composites Group, Polymers Division, Building 224, Room B108, National Institute of Standards and Technology, Gaithersburg, MD 20899, USA*

Received 30 July 1998; revised 19 August 1999; accepted 7 July 2000

Abstract

In the injection/compression liquid composite molding process (I/C-LCM), a liquid polymer resin is injected into a partially open mold, which contains a preform of reinforcing fibers. After some or all of the resin has been injected, the mold is closed, compressing the preform and causing additional resin flow. This paper addresses compression of the preform, with particular emphasis on modeling three-dimensional mold geometries and multi-layer preforms in which the layers have different mechanical responses. First, a new constitutive relation is developed to model the mechanical response of fiber mats during compression. We introduce a new form of nonlinear elasticity for transversely isotropic materials. A special case of this form is chosen that includes the compressive stress generated by changes in mat thickness, but suppresses all other responses. This avoids the need to model slip of the preform along the mold surface. Second, a finite element method, based on the principle of virtual displacement, is developed to solve for the deformation of the preform at any stage of mold closing. The formulation includes both geometric and material nonlinearities, and uses a full Newton–Raphson iteration in the solution. An open gap above the preform can be incorporated by treating the gap as a distinct material layer with a very small stiffness. Examples show that this approach successfully predicts compression in dry preforms for three-dimensional I/C-LCM molds.

Keywords: E: Injection moulding; E: Compression moulding; E: Resin transfer moulding; B: Anisotropy; A: Fibres; Nonlinear elasticity

1. Introduction

Injection/compression liquid composite molding (I/C-LCM) is a process for manufacturing polymer–matrix composites. As in other liquid composite molding processes, a preform of reinforcing fibers is placed in the mold, and a liquid resin is injected into the mold to saturate the preform. Curing the liquid resin provides a stiff, solid part. In I/C-LCM the mold is partially open during the initial stages of injection; this permits easier resin flow, due to higher porosity and permeability in the preform. After all of the resin has been injected, the mold is closed to its final position. This completes mold filling by compressing the preform and inducing additional resin flow. Compared to other LCM processes, I/C-LCM offers lower injection pressures and faster mold filling.

Numerical simulation has already proved to be an important tool for designing molds and selecting processing conditions for liquid composite molding. Resin flow through the porous fiber preform is modeled using the theory of flow through porous media, and there are well-established numerical methods for tracking the moving flow front and solving the flow equations in complex geometries [1–8].

In addition to the fluid mechanics of resin flow, a model of I/C-LCM must treat the solid mechanics of fiber mat compression. Several experiments have been done to characterize the compressibility of fiber mats, measuring their normal stress as a function of normal strain for a flat sample [9–12]. And some simulations of resin flow and preform deformation have been developed for injection/compression processes [13,14], again for flat parts with uniform thickness. However, practical problems can be quite complex, involving three-dimensinoal (3D) geometries as well as multiple reinforcement layers with different

* Corresponding author. Tel.: +1-217-333-2692; fax: +1-217-244-6534.
E-mail address: c-tucker@uiuc.edu (C.L. Tucker).
[1] Current address. Center for Composite Materials, University of Delaware, Newark, DE 19716, USA

1359-835X/01/$ - see front matter
PII: S1359-835X(00)00137-8

compressibilities and permeabilities. Some processes start with an open gap between the preform and the mold, and this gap gradually closes during the process. The goal of this work is to develop a simulation of I/C-LCM that can treat all of these factors.

In a previous paper [15] we showed how to generate a 3D, layered finite element mesh for the mold cavity, starting from the type of shell mesh that is typically used to represent part geometry in mold filling simulations. We also introduced the concept of separate finite element meshes for modeling preform deformation and resin flow. The *mechanical mesh*, used to calculate preform deformation, has one layer of elements for each reinforcement layer in the preform. At any stage of deformation this is automatically subdivided into multiple sub-layers to create the *flow mesh*, which is used to solve for the resin flow. We also developed the geometry and data structure for compressing the mesh as the mold closes. Each node in the 3D mesh sits on a *spine*, which is a vector connecting a node on the lower mold surface to a matching node on the upper mold surface. As the mold closes, the internal nodes slide up and down on their spines to adjust the shape of the mesh. This reduces the number of displacement degrees of freedom per node from three, as in a conventional solid mechanics problem, to a single parameter that describes the position of the node along the spine.

Building on that geometric treatment, this paper addresses the solid mechanics of preform deformation. A major assumption is that the deformation of the preform is not affected by the resin flow. That is, the drag force on the fibers from resin flow is too small to cause substantial deformation of the fiber preform. This assumption decouples the flow and preform deformation calculations, and allows us to treat the preform deformation as a purely mechanical problem.

In the first part of the paper we develop a general constitutive equation for modeling preform compression in the presence of large deformations and large rotations. Based on the theory of anisotropic finite-strain elasticity, this equation provides a rigorous foundation for treating preform deformation in complex mold geometries. The parameters for any specific material can be developed from flat-sample compression data, so no new experiments are required to characterize a preform material.

In the second part of the paper, a finite element solution, based on the theory of virtual displacement, is developed to solve preform deformation problems. The formulation includes both geometric and material nonlinearity, and the nonlinear equations are solved using a full Newton–Raphson scheme. The use of spines in this formulation, and the attendant reduction in nodal degrees of freedom, provides considerable savings in computation. Open gaps are incorporated naturally, by treating the gap as a separate layer of preform "material" which is much softer than the other layers, but stiffens rapidly as its thickness approaches zero. We present several examples to demonstrate the accuracy and capabilities of the method. In a subsequent paper [16] we combine this code with a finite element simulation of resin flow to provide a complete treatment of I/C-LCM.

2. A constitutive equation for fiber mat compression

2.1. Notation and kinematics

We begin by reviewing some basic aspects of large-strain kinematics. The preform material begins from a *reference configuration*, say at time equal to zero, while at time t it has some other deformed configuration. We will use a left superscript to indicate the time at which a quantity is evaluated. Thus, the Cartesian coordinates of any material point in the reference configuration are ${}^0\mathbf{x}$, while in the deformed configuration the same material point has coordinates ${}^t\mathbf{x}$. Now we assume that there is a smooth, invertible mapping between the reference and deformed states, ${}^t\mathbf{x} = {}^t\mathbf{x}({}^0\mathbf{x})$ or ${}^0\mathbf{x} = {}^0\mathbf{x}({}^t\mathbf{x})$. The derivatives of these functions are the deformation gradient tensors $\mathbf{F}$ and $\mathbf{F}^{-1}$, whose components are

$$F_{ij} = \frac{\partial {}^t x_i}{\partial {}^0 x_j} \qquad \text{and} \qquad F_{ij}^{-1} = \frac{\partial {}^0 x_i}{\partial {}^t x_j} \tag{1}$$

These tensors describe the shape change and solid-body rotation in the vicinity of any material point.

Using the deformation gradients, one can define finite deformation tensors that describe the local shape change, but are independent of the solid-body rotation. There are four such tensors,

$$\mathbf{C} = \mathbf{F}^{\mathrm{T}} \cdot \mathbf{F} \tag{2}$$

$$\mathbf{C}^{-1} = \mathbf{F}^{-1} \cdot \mathbf{F}^{-\mathrm{T}} \tag{3}$$

$$\mathbf{B} = \mathbf{F} \cdot \mathbf{F}^{\mathrm{T}} \tag{4}$$

$$\mathbf{B}^{-1} = \mathbf{F}^{-\mathrm{T}} \cdot \mathbf{F}^{-1} \tag{5}$$

where $\mathbf{F}^{-\mathrm{T}}$ stands for $(\mathbf{F}^{-1})^{\mathrm{T}}$. We will call these the Cauchy–Green, Piola, Finger and Al-mansi tensors, respectively. Each of these tensors has three scalar invariants. The invariants of the Piola tensor are

$$I_1 = \mathrm{tr}(\mathbf{C}^{-1}) \tag{6}$$

$$I_2 = \tfrac{1}{2}[(\mathrm{tr}\mathbf{C}^{-1})^2 - \mathrm{tr}(\mathbf{C}^{-1})^2] \tag{7}$$

$$I_3 = \det(\mathbf{C}^{-1}) \tag{8}$$

The corresponding invariants of $\mathbf{C}$ will be denoted by J_1, J_2 and J_3. We will also use the Green–Lagrange strain tensor $\boldsymbol{\epsilon}$, which is defined as

$$\boldsymbol{\epsilon} = \tfrac{1}{2}(\mathbf{C} - \boldsymbol{\delta}) \tag{9}$$

where $\boldsymbol{\delta}$ is the unit tensor.

If an infinitesimal material vector connects two neighboring material points, then that vector ${}^{t}\mathbf{p}$ in the deformed state in related to the same vector in the reference state ${}^{0}\mathbf{p}$ by

$${}^{t}\mathbf{p} = \mathbf{F}\cdot{}^{0}\mathbf{p} \tag{10}$$

Similarly, an infinitesimal material volume dV changes size according to

$$\mathrm{d}^{t}V = \det(\mathbf{F})\mathrm{d}^{0}V \tag{11}$$

An infinitesimal material area is described by two quantities, a magnitude dS and a unit normal vector $\mathbf{n}$. These transform according to

$$\mathrm{d}^{t}S = \det(\mathbf{F})\sqrt{{}^{0}\mathbf{n}\cdot\mathbf{C}^{-1}\cdot{}^{0}\mathbf{n}}\,\mathrm{d}^{0}S \tag{12}$$

$${}^{t}\mathbf{n} = \frac{\mathbf{F}^{-\mathrm{T}}\cdot{}^{0}\mathbf{n}}{\sqrt{{}^{0}\mathbf{n}\cdot\mathbf{C}^{-1}\cdot{}^{0}\mathbf{n}}} \tag{13}$$

The Cauchy stress, or true stress, will be denoted by $\mathbf{T}$. We will also make use of the first and second Piola–Kirchoff stress tensors, $\mathbf{P}$ and $\mathbf{S}$, respectively, which are related to $\mathbf{T}$ by

$$\mathbf{T} = \frac{1}{\det(\mathbf{F})}\mathbf{F}\cdot\mathbf{P} \tag{14}$$

$$\mathbf{T} = \frac{1}{\det(\mathbf{F})}\mathbf{F}\cdot\mathbf{S}\cdot\mathbf{F}^{\mathrm{T}} \tag{15}$$

2.2. Classical nonlinear elasticity

Returning to fiber preforms, we are interested in the deformation when woven fabrics or random-fiber mats are compressed in their thickness direction. These materials have a reasonably well-defined thickness in the unstressed state, and we take this as the reference configuration. Some typical stress–strain curves, when these materials are compressed between two flat plates, appear in Fig. 3. The thickness changes are comparable to the initial thickness, so this is clearly a large-strain problem. Also, there is no noticeable expansion in the lateral directions, so the fiber mats are being compressed volumetrically. Finally the stress–strain curves are highly nonlinear, so a nonlinear type of constitutive equation is required.

Here we choose to develop a constitutive framework using the theory of nonlinear elasticity. We note that the compressive response of fiber mats may not be purely elastic. In particular, a mat that is compressed and then released may exhibit some hysteresis. However, with few exceptions [17], there is little data that explores this inelastic response. More importantly, for I/C-LCM the compressive loading is always monotonic, so we do not need to describe the loading/unloading behavior, and a nonlinear elastic model is adequate.

Fiber preforms are also highly anisotropic, with very different structure and mechanical response in the in-plane and thickness direction. Since our problem is dominated by thickness-direction compression, we choose to develop a model that is transversely isotropic, with the plane of the sheet being the plane of material symmetry. This avoids a great deal of mathematical complexity by ignoring the in-plane anisotropy of woven fabrics.

The classical theory of large-strain elasticity is well documented in many books [18–20]. However, the treatment of anisotropic, compressible materials is less well known. Here we repeat a few of the key steps of the classical theory as presented by Lurie [20], to lay the groundwork for our own development. Some formulae used in this development are given in Appendix A.

A material is elastic (or hyperelastic) if it stores, as internal energy, all the work done on it. Such a the material must possess a scalar *strain energy function* $W(\mathbf{F})$, giving the energy per unit unstrained volume stored at the deformation state $\mathbf{F}$. Following Lurie (Chapter 4, Section 1), the change in stored energy for a change $\delta\mathbf{F}$ in deformation is

$$\delta W = \mathbf{P} : \delta\mathbf{F} \tag{16}$$

Comparing Eq. (16) to the definition of a derivative of a scalar with respect to a tensor, Eq. (A1), we find that the stress in an elastic body is given by

$$\mathbf{P} = \frac{\partial W}{\partial \mathbf{F}^{\mathrm{T}}} \tag{17}$$

For the constitutive equation to be objective, W must be independent of the solid-body rotation contained in $\mathbf{F}$, and hence must depend on quantities like the deformation tensors in Eqs. (2)–(5). Any one of these four tensors might be chosen, but the classical choice is to take W to be a function of $\mathbf{C}$. We can use Eqs. (2) and (A2) to replace $\partial W/\partial\mathbf{F}$ by $\partial W/\partial\mathbf{C}$. Then, using Eq. (14), we find that the Cauchy stress in an elastic material is given by

$$\mathbf{T} = \frac{2}{\det(\mathbf{F})}\mathbf{F}\cdot\frac{\partial W}{\partial \mathbf{C}}\cdot\mathbf{F}^{\mathrm{T}} \tag{18}$$

The scalar function W is said to be an *isotropic function* of the tensor $\mathbf{C}$ if the form of its functional dependence on $\mathbf{C}$ is unaltered by any orthogonal transformation of $\mathbf{C}$ (i.e. any rotation of the coordinate axes). Typically this property holds for some subgroup of all orthogonal transforms, and this subgroup determines the symmetry group (i.e. the type of anisotropy) of the material. If W is an isotropic function for *all* orthogonal transforms, then it corresponds to the properties of an isotropic material, and W must depend only on the invariants of $\mathbf{C}$, namely J_1, J_2 and J_3. If W is an isotropic function for all orthogonal transforms that preserve the direction of a single symmetry axis ${}^{0}\mathbf{p}$, then the material is *transversely isotropic*, and the functional form must be

$$W(\mathbf{C}) = W(J_1, J_2, J_3, \mathscr{L}, \mathscr{M}) \tag{19}$$

The additional scalars that characterize the strain state are

$$\mathscr{L} = {}^0\mathbf{p}\cdot\mathbf{C}\cdot{}^0\mathbf{p} \tag{20}$$

$$\mathscr{M} = {}^0\mathbf{p}\cdot\mathbf{C}^2\cdot{}^0\mathbf{p} \tag{21}$$

We now expand the derivative in Eq. (18) using the chain rule:

$$\frac{\partial W}{\partial \mathbf{C}} = \frac{\partial W}{\partial J_1}\frac{\partial J_1}{\partial \mathbf{C}} + \frac{\partial W}{\partial J_2}\frac{\partial J_2}{\partial \mathbf{C}} + \frac{\partial W}{\partial J_3}\frac{\partial J_3}{\partial \mathbf{C}} + \frac{\partial W}{\partial \mathscr{L}}\frac{\partial \mathscr{L}}{\partial \mathbf{C}} + \frac{\partial W}{\partial \mathscr{M}}\frac{\partial \mathscr{M}}{\partial \mathbf{C}} \tag{22}$$

This expression is substituted into Eq. (18), and simplified by introducing formulae for the derivatives of the invariants, Eq. (A4), and of $\mathscr{L}$ and $\mathscr{M}$, Eqs. (A5) and (A6). We also use Eq. (10) to transform ${}^0\mathbf{p}$ in the reference state to the vector ${}^t\mathbf{p}$ in the deformed state. That is, the material symmetry axis is assumed to deform like a material line. After some simplification, this gives the Cauchy stress as

$$\mathbf{T} = \frac{2}{\det(\mathbf{F})}\left\{\left(J_3\frac{\partial W}{\partial J_3}\right)\boldsymbol{\delta} + \left(\frac{\partial W}{\partial J_1} + J_1\frac{\partial W}{\partial J_2}\right)\mathbf{B} - \left(\frac{\partial W}{\partial J_2}\right)\mathbf{B}^2 + \left(\frac{\partial W}{\partial \mathscr{L}}\right){}^t\mathbf{p}\,{}^t\mathbf{p} + \left(\frac{\partial W}{\partial \mathscr{M}}\right)[{}^t\mathbf{p}\,{}^t\mathbf{p}\cdot\mathbf{B} + \mathbf{B}\cdot{}^t\mathbf{p}\,{}^t\mathbf{p}]\right\} \tag{23}$$

This is the classical constitutive equation for a hyperelastic material that is both compressible and transversely isotropic, and is the form given by Lurie [20] and by Green and Adkins [18]. The corresponding equation for an isotropic material can be recovered by omitting the last two terms. In this form the Cauchy stress is a function of the Finger strain tensor $\mathbf{B}$ and the instantaneous material symmetry axis ${}^t\mathbf{p}$, and the material properties are contained in the various derivatives of W. This treatment is highly appropriate when the anisotropy is induced by aligned fibers that are initially oriented parallel to ${}^0\mathbf{p}$. Since these fibers are embedded in the material, in the deformed state they will be oriented in the ${}^t\mathbf{p}$ direction. In particular, we can interpret the term containing $\partial W/\partial \mathscr{L}$ as a normal stress parallel to the fiber axis. Note that $\mathscr{L}$ measures the amount of stretching along the fiber axis.

2.3. A new constitutive equation

When modeling fiber mat compression during I/C-LCM, we take the plane of the mat as the plane of isotropy, and the vector normal to that plane as the material symmetry axis. If the mold compressed the mat only along that axis, then Eq. (23) might be quite suitable as a constitutive equation. However, for realistic part geometries there are often regions of the mold where the mold surfaces are not normal to the mold closing axis. In these regions, closing the mold not only compresses the preform, it also causes the moving surface to translate parallel to the plane of the sheet. This motion is probably taken up by slip between the outer preform layer and the mold surface. However, it is more convenient to build finite element meshes whose nodes are fixed on the mold surfaces than it is to model this slip explicitly, and these meshes experience some shear as the mold is closed. We would like to have a constitutive equation that is insensitive to this shear, but still models the thickness-direction compressive behavior of the mat. Eq. (23) is not suitable for this purpose, since the shearing motions keep ${}^t\mathbf{p}$ from being normal to the material symmetry plane.

A more appropriate constitutive equation can be developed by reformulating the transversely isotropic hyperelastic material, taking W to be a function of the Piola deformation tensor $\mathbf{C}^{-1}$. We will see later that this leads to a physically meaningful way to characterize the thickness-direction compression in the preform, but for now we simply note that this is an alternate formulation that is consistent with all the assumptions of the classical theory of nonlinear elasticity.

Using the derivative relation Eq. (A3), we find that the derivatives of W with respect to $\mathbf{C}$ and $\mathbf{C}^{-1}$ are related by

$$\frac{\partial W}{\partial \mathbf{C}} = -\mathbf{C}^{-1}\cdot\frac{\partial W}{\partial \mathbf{C}^{-1}}\cdot\mathbf{C}^{-1} \tag{24}$$

(Note that $\mathbf{C}^{-1}$ is symmetric.) This result can be combined with Eqs. (18) and (3) to given the Cauchy stress as

$$\mathbf{T} = -\frac{2}{\det(\mathbf{F})}\mathbf{F}^{-\mathrm{T}}\cdot\frac{\partial W}{\partial \mathbf{C}^{-1}}\cdot\mathbf{F}^{-1} \tag{25}$$

Since the material is transversely isotropic, the strain energy function must depend on the invariants of $\mathbf{C}^{-1}$ and on two new scalars, L and M:

$$W(\mathbf{C}^{-1}) = W(I_1, I_2, I_3, L, M) \tag{26}$$

$$L = {}^0\mathbf{n}\cdot\mathbf{C}^{-1}\cdot{}^0\mathbf{n} \tag{27}$$

$$M = {}^0\mathbf{n}\cdot(\mathbf{C}^{-1})^2\cdot{}^0\mathbf{n} \tag{28}$$

Here ${}^0\mathbf{n}$ is a unit vector parallel to the material symmetry axis in the undeformed state. As before, we expand $\partial W/\partial \mathbf{C}^{-1}$ using the chain rule, substitute for the derivatives of the invariants with respect to $\mathbf{C}^{-1}$ and return the result to the stress Eq. (25). However, this time the natural simplification is that $\mathbf{n}$ transforms between the reference and deformed states like the normal to a material surface. That is, ${}^t\mathbf{n}$ and ${}^0\mathbf{n}$ are related by Eq. (13). In fact, the denominator on the right-hand side of Eq. (13) is the square root of L, so the relationship is quite simple. After a good deal of simplification, we obtain the Cauchy stress as

$$\mathbf{T} = -\frac{2}{\det(\mathbf{F})}\left\{\left(I_3\frac{\partial W}{\partial I_3}\right)\boldsymbol{\delta} + \left(\frac{\partial W}{\partial I_1} + I_1\frac{\partial W}{\partial I_2}\right)\mathbf{B}^{-1} - \left(\frac{\partial W}{\partial I_2}\right)(\mathbf{B}^{-1})^2 + \left(L\frac{\partial W}{\partial L}\right){}^t\mathbf{n}\,{}^t\mathbf{n} + \left(L\frac{\partial W}{\partial M}\right)[{}^t\mathbf{n}\,{}^t\mathbf{n}\cdot\mathbf{B}^{-1} + \mathbf{B}^{-1}\cdot{}^t\mathbf{n}\,{}^t\mathbf{n}]\right\} \tag{29}$$

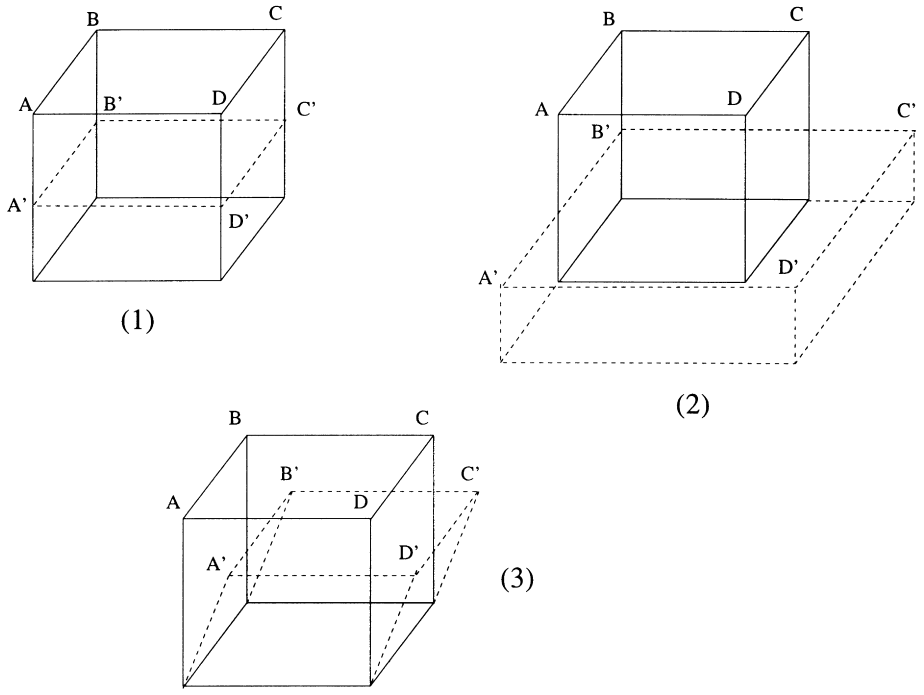

Fig. 1. Three different types of deformation of a cubic element. ABCD and A′B′C′D′ are the upper edges of the undeformed and deformed element, respectively: (a) the element is compressed in the thickness direction only; (b) the element is compressed in the thickness direction and stretched in the plane; and (c) the element is compressed and sheared parallel to the plane.

This is, as far as we know, a new form for the stress in a transversely isotropic, hyperelastic material. Comparing it to Eq. (23), we see that here the stress is a function of the Almansi deformation tensor $\mathbf{B}^{-1}$ and the vector ${}^t\mathbf{n}$, which we interpret as the instantaneous normal to the plane of material symmetry. Note that ${}^0\mathbf{p}$ and ${}^0\mathbf{n}$ are coaxial; that is, the material symmetry axis is normal to the material symmetry plane in the reference state. However, for the deformed state ${}^t\mathbf{p}$ and ${}^t\mathbf{n}$ are *not* necessarily coaxial. A finite deformation can result in a material symmetry axis that is no longer normal to the material symmetry plane. Eq. (29) is most suitable for a material whose transverse isotropy is associated with a *plane* of material symmetry, in our case the plane of the fiber mat.

Since Eq. (29) was derived from the same assumptions as the classical Eq. (23), the two forms are, in principal, equivalent. That is, for any set of material properties used in Eq. (29), there should exist some set of material properties that could be used in Eq. (23) to produce identical behavior. The utility of Eq. (29) is that useful, simple forms can be found by omitting selected terms. We note that the term containing $\partial W/\partial L$ is a normal stress acting on the material symmetry plane. This is the major effect we wish to capture, so we specialize Eq. (29) by choosing $W = W(L)$, so that

$$\frac{\partial W}{\partial I_1} = \frac{\partial W}{\partial I_2} = \frac{\partial W}{\partial I_3} = \frac{\partial W}{\partial M} = 0 \tag{30}$$

This reduces the constitutive equation to

$$\mathbf{T} = -\frac{2L}{\det(\mathbf{F})}\frac{\partial W}{\partial L}\,{}^t\mathbf{n}{}^t\mathbf{n} \tag{31}$$

For a physical interpretation of this model, consider an incremental material volume d^0V that, in the reference configuration, is a rectangular parallelepiped, with two surfaces that are parallel to the material symmetry plane. Let the area of one of these surfaces be d^0S. The height ${}^0h$ of this incremental volume, measured in the direction normal to d^0S, is equal to

$${}^0h = \mathrm{d}^0V/\mathrm{d}^0S \tag{32}$$

If the material is deformed, then a similar equation relates the height th to the volume d^tV and area d^tS in that configuration. A convenient measure of thickness change in the direction normal to the material symmetry plane is the ratio of these two heights,

$$\kappa = \frac{{}^th}{{}^0h} = \frac{\mathrm{d}^tV/\mathrm{d}^tS}{\mathrm{d}^0V/\mathrm{d}^0S} \tag{33}$$

We can generalize this idea using Eqs. (11) and (12), defining κ for any deformation as:

$$\kappa \equiv \frac{1}{\sqrt{{}^0\mathbf{n}\cdot\mathbf{C}^{-1}\cdot{}^0\mathbf{n}}} \tag{34}$$

κ functions like a stretch ratio, but it measures the change in separation of two parallel material planes, rather than the change in length of a line element. Note that κ measures

deformation relative to a specific material plane, the plane normal to ${}^0\mathbf{n}$.

Comparing Eq. (34) to Eq. (27), we see that

$$L = \frac{1}{\kappa^2} \tag{35}$$

so L and κ are equivalent measures of deformation. Since κ admits a simple physical interpretation, we can make W a function of κ, and write our constitutive equation as

$$\mathbf{T} = \frac{\kappa}{\det(\mathbf{F})}\frac{\partial W}{\partial \kappa}{}^t\mathbf{n}{}^t\mathbf{n} \tag{36}$$

This is the final form of our proposed constitutive equation. Specific material models are created by choosing $W(\kappa)$.

To explore the behavior of this equation, consider the three deformation states shown in Fig. 1. In all cases ABCD is a material symmetry plane in the reference configuration, and both ${}^0\mathbf{n}$ and ${}^t\mathbf{n}$ are parallel to the x_3 axis. Thus, in all cases the only stress present is T_{33}. The simple uniaxial compression in Fig. 1(a) and the combined compression and shear in Fig. 1(c) give the same values of κ and the same deformed volume, so both deformations produce the same T_{33}. This insensitivity to shearing parallel to the material symmetry plane is the quality that we sought in the constitutive equation. Fig. 1(b) shows a compression along the material symmetry axis, combined with spreading in the 1–2 plane. This also has the same value of κ as parts (a) and (c), but has a different value of $\det(\mathbf{F})$. Hence, T_{33} for this case will be lower than the other two cases. In fact, case (b) has the same total force in the x_3 direction as cases (a) and (b), but this force is spread over a larger area. Our rigorous constitutive derivation has provided a treatment of volume change that is consistent with our other assumptions of elastic behavior.

Some care must be taken when using Eq. (36) to solve boundary-value problems, for instance by the finite element method. Several modes of deformation, such as shearing parallel to the material symmetry plane, produce no change in internal energy for this model. In effect, the material has no stiffness to resist these deformation modes. Thus, if some external factor is not present to constrain these modes, the finite element equations will be singular and the problem will not have a unique solution. One could remove this singularity by adding small amounts of the isotropic terms (the first three terms) from Eq. (29) back into the constitutive equation. However, in our case the requisite constraints are provided by using the spines to limit the motion of the nodes in the finite element mesh, so we can use Eq. (36) without any modification.

2.4. Fitting experimental data

To obtain a specific form for Eq. (36) we need to choose a functional form for $W(\kappa)$, or alternately for $\partial W/\partial\kappa$. Uniaxial compression experiments are typically used to characterize the compressibility of fiber mats [10–12]. During such an experiment, a material element undergoes a deformation like Fig. 1(a), for which the coordinate transformation is

$${}^tx_1 = {}^0x_1 \qquad {}^tx_2 = {}^0x_2 \qquad {}^tx_3 = \alpha\,{}^0x_3 \tag{37}$$

Using Eqs. (1) and (3), the kinematic quantities are

$$\mathbf{F} = \begin{bmatrix} 1 & 0 & 0 \\ 0 & 1 & 0 \\ 0 & 0 & \alpha \end{bmatrix} \quad \mathbf{F}^{-1} = \begin{bmatrix} 1 & 0 & 0 \\ 0 & 1 & 0 \\ 0 & 0 & 1/\alpha \end{bmatrix}$$
$$\mathbf{C}^{-1} = \begin{bmatrix} 1 & 0 & 0 \\ 0 & 1 & 0 \\ 0 & 0 & 1/\alpha^2 \end{bmatrix} \quad \det(\mathbf{F}) = \alpha \tag{38}$$

With this value of $\mathbf{C}^{-1}$ and with ${}^0\mathbf{n} = {}^t\mathbf{n} = \langle 0, 0, 1\rangle$, Eq. (34) yields $\kappa = \alpha$. Then from Eq. (36) we find that $T_{ij} = 0$, except for

$$T_{33} = \frac{\partial W}{\partial \kappa} \tag{39}$$

In an experiment one measures T_{33} as a function of $\kappa(= {}^th/{}^0h)$, and a typical plot looks like Fig. 3.

Fitting experimental data simply requires choosing an appropriate form for $\partial W/\partial\kappa$ and adjusting the parameters of this form to fit the data. Several different functions have been used to fit compression data for fiber mats [10–12,21]. Our calculations use a form suggested by Trevino et al. [9], which yields

$$\frac{\partial \mathrm{W}}{\partial \kappa} = -10^{((\log(V_{\mathrm{f0}}/\kappa)+C)/D)} + 10^{((\log(V_{\mathrm{f0}})+C)/D)} \tag{40}$$

V_{f0} is the fiber volume fraction of the mat at its initial uncompressed state ($\kappa = 1$), while C and D are constants adjusted to fit the data. The second term on the right-hand side of Eq. (40) is added to the original form of Trevino et al. to give $T_{nn} = 0$ at $\kappa = 1$. The finite element equation also need the second derivative of W, which is

$$\frac{\partial^2 \mathrm{W}}{\partial \kappa^2} = \frac{1}{\kappa D}10^{((\log(V_{\mathrm{f0}}/\kappa)+C)/D)} \tag{41}$$

In some parts there is a gap between the top of the preform and the upper mold surface in the initial configuration. These gaps are modeled as a layer of a special material, which develop very little stress at finite thickness, but which stiffens dramatically as it is approaches zero thickness. After some trial and error, the following expression was found to exhibit the desired behavior:

$$\frac{\partial W}{\partial \kappa} = \frac{a^{3/2}}{1-\sqrt{a}}\left(1 - \frac{1}{\kappa}\right) \tag{42}$$

Here a is constant that must fall between 0 and 1. We typically use $a = 1.0 \times 10^{-4}$.

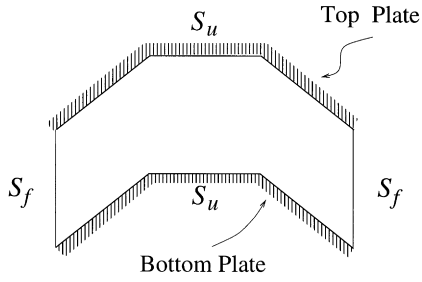

Fig. 2. Boundary conditions: there is no traction ($\mathbf{f}^S = 0$) on surface S_f, and zero virtual displacement ($\delta\mathbf{u} = 0$) on surface S_u.

3. Finite element procedures

3.1. Notation

Discussion of the finite element solution requires a great many superscripts and subscripts, for which we follow the conventions of Bathe [22]. As in the previous section, a left superscript indicates the time at which a quantity is evaluated. For quantities that depend both on the current configuration and a reference configuration, the time of the reference configuration indicated by a left subscript. Thus, the displacement gradient at time t with respect to a reference state at time 0, which was $\mathbf{F}$ in the previous section, is now written as ${}_0{}^t\mathbf{F}$, while ${}_t{}^{t+\Delta t}\mathbf{F}$ represents the displacement gradient at time $t + \Delta t$ with respect to a reference state at time t.

Right subscripts will indicate the Cartesian components of vectors and tensors, and a repeated index will imply summation over the appropriate range.

A lower-case right superscript will indicate the node number of a nodal quantity; summation over these indices will always be written out explicitly. Right superscripts B and S indicate body and surface quantities, respectively. When discussing iterative solutions, right superscripts in parentheses will indicate the iteration number.

3.2. Nodal degrees of freedom

The first paper in the series [15] introduced the use of spines to control the deformation of the 3D finite elements mesh. Each node k is associated with a spine vector $\mathbf{s}^k$, which has unit length. The base of the spine vector resides at a fixed position $\mathbf{X}^k$, which corresponds to a node on the (fixed) lower surface of the mold. The position of the node along the spine is controlled by a scalar spine parameter λ^k, such that at any time t the position of the node is given by

$$ {}^t\mathbf{x}^k = \mathbf{X}^k + {}^t\lambda^k {}^t\mathbf{s}^k \tag{43}$$

Using Eq. (43), the displacement of a node can be expressed as:

$$ {}^t u_i^k = {}^t\lambda^k\, {}^t s_i^k - {}^0\lambda^k\, {}^0 s_i^k \tag{44}$$

where the left superscript 0 indicates the initial state. In an I/C-LCM process the closing of the mold is prescribed, so the position of the upper mold surface at each time step is known. As a result, both of the spine vectors ${}^t s_i^k$ and ${}^0 s_i^k$ are known. The initial spine parameter ${}^0\lambda^k$ is also known, being calculated as part of the initial construction of the mechanical mesh [15]. Therefore, the current spine parameter ${}^t\lambda^k$ is the only unknown in this expression for the displacement. The unknown spine parameters for all the nodes are the primary variables in our formulation.

3.3. Principle of virtual work

Our starting point for deriving the finite element equations is the principle of virtual work. This principle states that a body is in equilibrium at time $t + \Delta t$ if, for a small, imaginary "virtual" displacement field $\delta u_i(x_j)$, the internal work on the body equals the external work (e.g. Ref. [22]):

$$\int_{{}^{t+\Delta t}V} {}^{t+\Delta t}T_{ij}\, \delta_{t+\Delta t} e_{ij}\, \mathrm{d}^{t+\Delta t}V = \int_{{}^{t+\Delta t}V} {}^{t+\Delta t}f_i^B\, \delta u_i\, \mathrm{d}^{t+\Delta t}V + \int_{{}^{t+\Delta t}S_f} {}^{t+\Delta t}f_i^S\, \delta u_i^S\, \mathrm{d}^{t+\Delta t}V \tag{45}$$

The virtual displacement field must be zero at all points where the displacement of the body is prescribed, but is otherwise arbitrary. In this equation

$$ \delta_{t+\Delta t} e_{ij} = \frac{1}{2}\left(\frac{\partial \delta u_i}{\partial {}^{t+\Delta t}x_j} + \frac{\partial \delta u_j}{\partial {}^{t+\Delta t}x_i} \right) \tag{46}$$

represents the infintesimal strain tensor corresponding to virtual displacements, ${}^{t+\Delta t}V$ is the volume of the body at time $t = \Delta t$, ${}^{t+\Delta t}S_f$ is the part of the body's surface where surface traction boundary conditions are applied, and ${}^{t+\Delta t}f_i^B$ and ${}^{t+\Delta t}f_i^S$ are the prescribed body force and surface tractions, respectively.

For our problem the body force f_i^B is negligible. The boundary conditions, as shown in Fig. 2, involve either a prescribed displacement (on the mold surfaces) or zero surface traction f_i^S (along the edges of the preform). Hence, the right-hand side of Eq. (45) is zero, and we neglect it from this point onward.

The left-hand side of Eq. (45) must be treated carefully, since in a large-deformation problem we do not know the deformed configuration ${}^{t+\Delta t}V$. We choose to use the updated Lagrangian formulation. Suppose for the moment that we know the displacements and stresses at time t, and we wish to solve for the displacements at time $t + \Delta t$. The left-hand side of Eq. (45) can be transformed into an integral over the shape at time t, using Eqs. (15) and (9) to replace the Cauchy stress with the second Piola–Kirchoff stress, and the infinitesimal strain with the Green–Lagrange strain. After some cancellation (see Ref. [22]), we find the principle of virtual work to be

$$\int_{{}^tV} {}^t{}^{t+\Delta t}S_{ij}\, \delta_t \epsilon_{ij}\, \mathrm{d}^t V = 0 \tag{47}$$

Table 1
Parameters for the strain energy density function, Eq. (40), to give stress in N/m^2

Fiber mat	V_{f0}	C	D
Random mat	0.15	0.0916	0.2832
Unidirectional mat	0.25	1.057	0.1031
Bidirectional mat	0.30	1.177	0.0954

Here ${}_t\epsilon_{ij}$ is the increment in the Green–Lagrange strain tensor between t and $t + \Delta t$,

$$ {}_t\epsilon_{ij} = \frac{1}{2}\left(\frac{\partial u_i}{\partial {}^t x_j} + \frac{\partial u_j}{\partial {}^t x_i} + \frac{\partial u_k}{\partial {}^t x_i}\frac{\partial u_k}{\partial {}^t x_j} \right) \tag{48} $$

with u_i, denoting the displacement increment,

$$ u_i \equiv {}^{t+\Delta t}u_i - {}^t u_i \tag{49} $$

We generate an equilibrium equation for each of the n_{nodes} nodes in the mesh by creating n_{nodes} different virtual displacement fields, each one corresponding to the perturbation of a different spine parameter $\delta\lambda^l$. Then we can make replacements like $\delta_t\epsilon_{ij} = (\partial_t\epsilon_{ij}/\partial\lambda^l)\delta\lambda^l$. The perturbation $\delta\lambda^l$ is independent of position and can be brought outside the integral. Then, since the equation must hold for arbitrary virtual dispacements, the $\delta\lambda^l$'s can be canceled from the equation. We are now left with a set of equilibrium equations,

$$ {}^{t+\Delta t}R^l \equiv \int_{{}^tV} {}^t{}^{t+\Delta t}S_{ij}\frac{\partial_t\epsilon_{ij}}{\partial^t\lambda^l}\,\mathrm{d}^tV = 0 \tag{50} $$

where ${}^{t+\Delta t}R^l$ is the residual for node l.

3.4. Newton–Raphson iteration

To find an increment in the spine parameters $\mathrm{d}^t\lambda^m$ that will make each ${}^{t+\Delta t}R^l$ equal to zero, we expand the residual in a Taylor series about time t:

$$ {}^{t+\Delta t}R^l \approx {}^tR^l + \sum_{m=1}^{n_{\text{nodes}}}\frac{\partial^tR^l}{\partial^t\lambda^m}\mathrm{d}^t\lambda^m \tag{51} $$

We equate this expression to zero, and find the increment by solving

$$ \sum_{m=1}^{n_{\text{nodes}}}\frac{\partial^tR^l}{\partial^t\lambda^m}\mathrm{d}^t\lambda^m = -{}^tR^l \tag{52} $$

We then update the solution as ${}^{t+\Delta t}\lambda^m = {}^t\lambda^m + \mathrm{d}^t\lambda^m$.

The resiual ${}^tR^l$ is evaluated by letting $t + \Delta t \to t$ in Eq. (50). Note that this gives

$$ {}^{t+\Delta t}_tS_{ij} = {}^tT_{ij} \tag{53} $$

Using this in Eq. (50), the tangent stiffness matrix is calculated as

$$ \frac{\partial^tR^l}{\partial^t\lambda^m} = \int_{{}^tV}\frac{\partial^tT_{ij}}{\partial^t\lambda^m}\frac{\partial_t\epsilon_{ij}}{\partial^t\lambda^l}\mathrm{d}^tV + \int_{{}^tV}{}^tT_{ij}\frac{\partial^2{}_t\epsilon_{ij}}{\partial^t\lambda^l\,\partial^t\lambda^m}\mathrm{d}^tV \tag{54} $$

Owing to the nonlinearity of the problem, a single update based on Eqs. (52) and (54) does not produce an adequate solution, and multiple iterations are required. The first iteration uses the equations developed so far, while all subsequent iterations linearize about the most recent trial configuration, say at time $t + \Delta t$ and iteration (p), to find iteration $(p + 1)$. Thus, our final algorithm is to solve for an increment in the spine parameters using

$$ \sum_{m=1}^{n_{\text{nodes}}}{}^{t+\Delta t}K^{lm,(p)}\,\mathrm{d}^{t+\Delta t}\lambda^{m,(p)} = -{}^{t+\Delta t}R^{l,(p)} \tag{55} $$

and then update the solution using

$$ {}^{t+\Delta t}\lambda^{m,(p+1)} = {}^{t+\Delta t}\lambda^{m,(p)} + \mathrm{d}^{t+\Delta t}\lambda^{m,(p)} \tag{56} $$

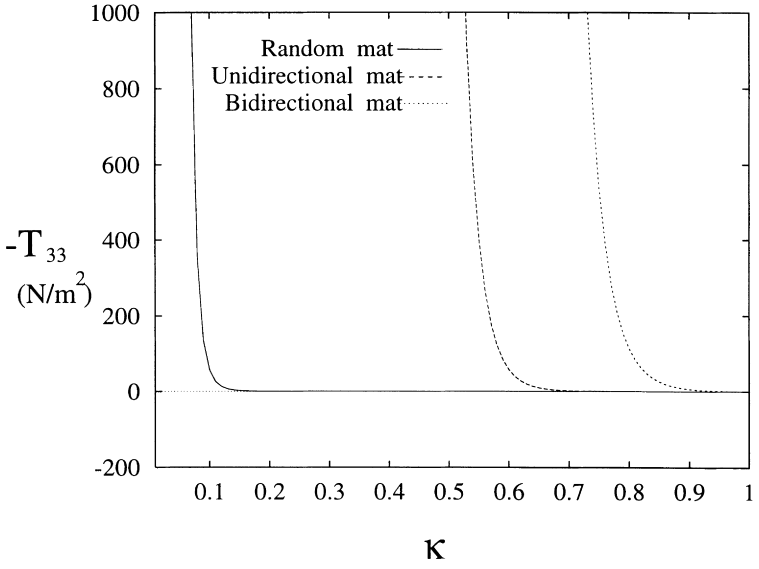

Fig. 3. Plot of compressive stress, T_{33}, against compressive strain κ = (deformed thickness/initial thickness) for random, unidirectional and bidirectional fiber mats. The curves are based on Eq. (40) and Table 1.

Table 2
Comparison of the final thickness (in cm) predicted by the analytical and numerical solutions for a three-layer preform

Fiber mat	Analytical prediction	Numerical prediction	% Error
Bidirectional (B)	0.07833	0.07837	+ 0.05
Unidirectional (U)	0.04335	0.04323	− 0.28
Bidirectional (B)	0.07833	0.07837	+ 0.05

Here the tangent stiffness matrix and the residual vector at iteration (p) are given by

$$ {}^{t+\Delta t}K^{lm,(p)} = \left[\int_{{}^{t+\Delta t}V} \left(\frac{\partial^{t+\Delta t}T_{ij}}{\partial^{t+\Delta t}\lambda^m} \frac{\partial_{t+\Delta t}\epsilon_{ij}}{\partial^{t+\Delta t}\lambda^l} + {}^{t+\Delta t}T_{ij} \frac{\partial^2{}_{t+\Delta t}\epsilon_{ij}}{\partial^{t+\Delta t}\lambda^m \partial^{t+\Delta t}\lambda^l} \right) \mathrm{d}^{t+\Delta t}V \right]^{(p)} \quad (57) $$

$$ {}^{t+\Delta t}R^{l,(p)} = -\left[\int_{{}^{t+\Delta t}V} {}^{t+\Delta t}T_{ij} \frac{\partial_{t+\Delta t}\epsilon_{ij}}{\partial^{t+\Delta t}\lambda^l} \mathrm{d}^{t+\Delta t}V \right]^{(p)} \quad (58) $$

The converged solution at the previous time t provides the initial guess, and iterations proceed until the norms of both the residual vector ${}^{t+\Delta t}R^l$ and the solution increment vector ${}^{t+\Delta t}\lambda^l$ are smaller than pre-set tolerances.

The quantites in Eqs. (57) and (58) are evaluated by Gaussian quadrature. In our implementation the elements are eight-node bricks, and we use $2\times2\times2$ quadrature. We also use a six-node wedge element where we employ 7×2 quadrature. The reason for using these integration schemes is to keep the degree of precision at least 3 [22]. The derivatives of the Cauchy stress ${}^{t+\Delta t}T_{ij}$ and the strain increment ${}_{t+\Delta t}\epsilon_{ij}$ with respect to the spine parameters must be computed at each integration point for each iteration, a process that is straight-forward but tedious. Detailed formulae for these derivatives are given in Appendices B and C.

4. Results and discussion

The focus of the present work is to predict the deformation of a dry preform in a multi-step compression process. In the following examples we use three different types of fiber mat: random, bidirectional and unidirectional. The strain energy function used to represent these mats is given in Eq. (40), and the specific parameters for each mat appear in Table 1. These parameters are representative of the properties reported in the literature for each type of mat. Fig. 3 shows the stress–strain curves corresponding to these properties. The bidirectional mat is the stiffest, and the random mat is the most compliant. Some examples also have an open gap, which is treated as a separate "material" using the strain energy function in Eq. (42).

4.1. Inhomogeneous layers

First we compare our finite element results with a problem that can be solved analytically. Consider a three-layer preform in a flat, rectangular mold. The layers consist of unidirectional (U) and bidirectional (B) fiber mats, stacked in the sequence B–U–B. When the upper plate of

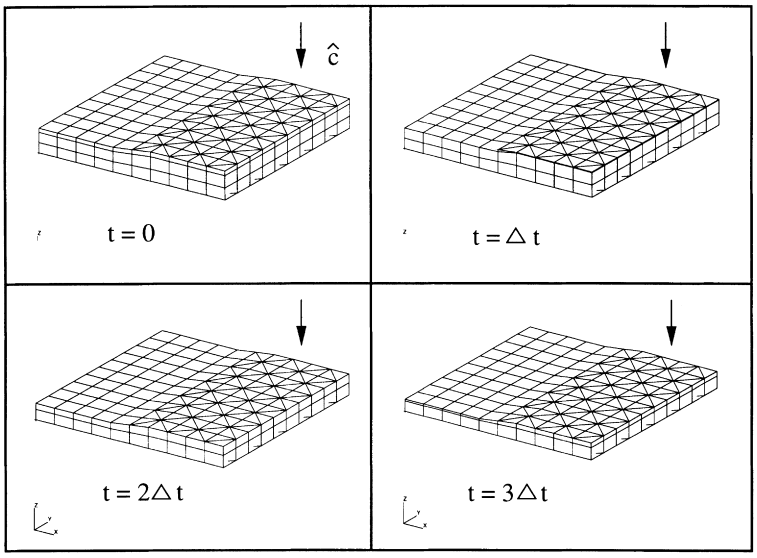

Fig. 4. Compression of a two-layer preform in a flat rectangular I/C-LCM mold. The upper layer of the preform consists of random mat and the lower layer consists of unidirectional mat; the top-most layer at $t = 0$ is the gap. The mold has different thickness in the two halves, which is meshed by the brick and wedge elements. **c** is the clamping direction.

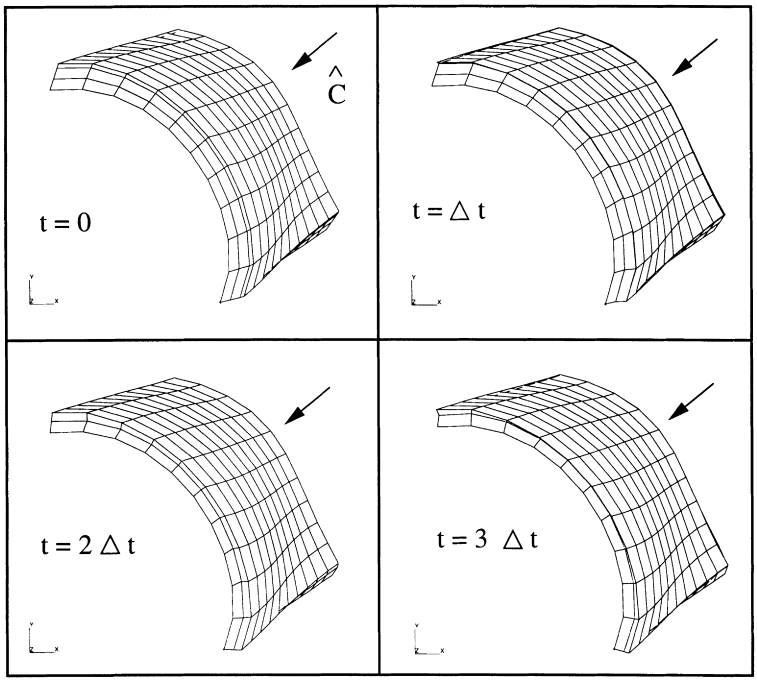

Fig. 5. Compression of a two-layer preform in a 3D mold. The upper layer of the preform consists of random mat and the lower layer consists of unidirectional mat; the top-most layer at $t = 0$ is the gap. **c** is the clamping direction.

the mold moves downwards, the preform compresses like three springs in series. The compressive stress is the same in all the three layers, and each layer deforms according to its own stress-strain curve. In this example the preform is compressed from an initial thickness of 0.3 cm (each layer is 0.1 cm thick) to a final thickness of 0.2 cm, and the final thickness of the three layers are to be determined. Using Eqs. (39) and (40), the compressive stress in any of the three layers is given by

$$T_{33} = -10^{((\log[V_{f0}{}^0h/{}^th]+C)/D)} + 10^{((\log V_{f0}+C)/D)} \quad (59)$$

Material constants V_{f0}, C and D for the layers are listed in Table 1, and ${}^0h$ is the given initial thickness of the layer. Note that the compressive stress for a layer is a function of the final thickness of the layer only, i.e. $T_{33} = T_{33}({}^th)$. The analytical solution is obtained by solving three simultaneous equations for the final thickness of the three layers: two from the equality of stresses in the layers and a third setting the sum of final layer thickness to 0.2 cm. Table 2 lists the final thickness of each layer as given by the analytical and numerical solutions. As expected, the uniaxial layer compresses more than the biaxial layers. There is a good match between the analytical and numerical results, the maximum error being less than 0.3%.

4.2. Planar mold with varying thickness and open gap

The second example is a flat, rectangular 1×1 m^2 mold divided into two regions with different thickness. The perform itself consists of a lower layer of unidirectional mat and an upper layer of random mat, the layers having equal initial thickness. The preform has a total initial thickness of 10 cm in the thinner region of the mold and 12 cm in the thicker region[2]. Initially there is an open gap between the top preform layer and the upper mold surface, and the thickness of the gap are 2 and 2.5 cm in the thinner and thicker regions, respectively.

The mechanical mesh for this problem is shown in Fig. 4. Two regions of the mold are represented by brick and wedge elements, respectively[3]. The shell mesh used to generate this mechanical mesh appears in Fig. 7 of Ref. [15]. The mesh generation algorithm enforces a continuous thickness, so the mold thickness change occurs gradually over two rows of elements, rather than as a sharp step. Our finite element formulation also enforces continuity of displacement in the interior of the mesh.

We now close the mold such that the top mold plate traverses 6 cm along the z axis. In principle it should be possible to compress the mold in one large step, but because of the limited radius of convergence of the Newton–Raphson scheme the process is accomplished in three equal time steps of size Δt. As the speed of the top plate is taken as a constant, it travels 2 cm in each time step. The mechanical compression process is unaffected by the mold closing

speed and the actual size of the time step is unimportant. Only the position of the upper mold enters the finite element calculation at each step.

Examining the results in Fig. 4, we see that the gap above the preform disappears in the first time step. The elements that represent the gap are still present, and have a small but finite thickness from this point onward. This allows our simulation to handle gap compression without implementing a separate contact algorithm, and without removing or deactivating elements during the simulation. In the second and third steps, the upper, more compliant random mat is compressed significantly more than the stiffer unidirectional layer on the bottom. This matches our expectation that more compliant fiber mats will take up most of the deformation when stacked with stiffer mats.

Performing a variety of simulations like this example, we found some cases that produced physical unrealistic results. When the initial thickness of a layer was very different between the two regions of the mold, our code predicted wiggles in the interfaces between layers. The constitutive relation, Eq. (36), mandates that the principal axis of the stress tensor be aligned with the material normal of the preform. At the mold surface the material normal is identical to the surface normal, so the traction applied by the mold plate on the preform is always normal to the mold surface at the point of contact. In a mesh like Fig. 4, the traction from the upper mold plate has an in-plane component in the region where mold thickness is changing, while the lower mold surface applies traction in the z direction only. The in-plane force from the upper mold is not balanced by any other external force, and must be absorbed as a reaction force by the constraints on nodal displacement. The material itself has no stiffness to resist the corresponding shear stresses, so as this force is transmitted through the mesh some irregularity in the deformation occurs. This is not a particularly serious problem, since the initial thickness of the preform layers is likely to be uniform across the mold, and a step change in thickness is not attractive from a structural viewpoint.

4.3. Arbitrary 3D mold

Finally, we consider a mold that is curved in three dimensions. The particular mesh was created from the shell mesh of an arbitrary surface patch (Fig. 11 of Ref. [15]). Once again, we consider a two-layer preform with a random mat at the top and a unidirectional mat at the bottom. Now there is only one material region in the mold, and the initial layer thickness is 3 cm everywhere. There is also an open gap at the top of the mold. The mold closes along the $\langle -1, -1, -1\rangle$ direction, and we show results for three time steps.

The initial mesh and the results are shown in Fig. 5, where **c** indicates the clamping axis. In the initial mesh the layers have uniform thickness. In the first step the open gap compresses to near-zero thickness over most of the mold. At the second step there is significant compression of the upper layer of random mat. In the third step the lower layer of bidirectional mat hardly compresses at all, while the random mat is highly compressed near the center of the mold, but still has significant thickness near the top and bottom edges. This is a consequence of the way that local cavity thickness changes with time in a 3D compression mold. This example demonstrates the ability of our simulation to capture the complex interactions between mold closing, mold geometry, open gaps and nonlinear material properties that are inherent in I/C-LCM.

5. Summary

To predict preform deformation during I/C-LCM a model must address several issues: the three-dimensional geometry of the mold, nonlinear properties of the preform, large deformation behavior and open gaps between the preform and the mold. We have developed techniques for treating all of these issues. The mold geometry is represented by a 3D finite element mesh. A special data structure attaches each node to a spine, and uses a single degree of freedom to move the node along the spine. We have developed a special constitutive equation to represent the mechanical response of the preform. This equation accommodates a wide variety of empirical equations for the stress–strain behavior in a simple compression test, and allows those expressions to be used in problems with large deformations and large rotations. The stress calculated by this equation is unaffected by shearing parallel to the plane of material symmetry, a feature that avoids spurious results when modeling I/C-LCM preforms. We have also developed finite element equations and solution methods for this highly nonlinear problem. The finite element formulation incorporates both material and geometric nonlinearities. Open gaps are treated as a separate layer of material, which has much lower stiffness than the preform layers, but which stiffens dramatically as its thickness approaches zero. Example calculations show that this approach can model nonuniform material properties, open gaps and molds with complex shapes.

This paper has focused on modeling the deformation of dry preforms. The next step is to combine this model with calculations of resin flow during injection/compression molding, to have a complete simulation of the process. We will report on this in a future publication [16].

Acknowledgements

Financial support for this work was provided by the National Institute of Standards and Technology.

Appendix A. Scalar functions of a tensor argument

To support the development of the constitutive equation,

we quote some basic mathematical results for a function $\phi(\mathbf{Q})$, where ϕ is scalar and $\mathbf{Q}$ is an arbitrary tensor. These results are discussed in more detail in Appendix 2 of Ref. [20].

The derivative $\partial\phi/\partial\mathbf{Q}$ is defined such that the change $\delta\phi$ produced by a change in argument $\delta\mathbf{Q}$ is

$$\delta\phi = \frac{\partial\phi}{\partial\mathbf{Q}} : \delta\mathbf{Q}^{\mathrm{T}} \tag{A1}$$

Note that $\partial\phi/\partial\mathbf{Q}$ is a tensor of the same order as $\mathbf{Q}$.

If one changes the argument of ϕ to $(\mathbf{Q}\cdot\mathbf{Q}^{\mathrm{T}})$ or to $\mathbf{Q}^{-1}$, then the derivatives are related by

$$\frac{\partial\phi}{\partial\mathbf{Q}} = 2\frac{\partial\phi}{\partial(\mathbf{Q}\cdot\mathbf{Q}^{\mathrm{T}})}\cdot\mathbf{Q} \tag{A2}$$

$$\mathbf{Q}^{\mathrm{T}}\cdot\frac{\partial\phi}{\partial\mathbf{Q}} = -\frac{\partial\phi}{\partial(\mathbf{Q}^{-1})}\cdot\mathbf{Q}^{-\mathrm{T}} \tag{A3}$$

The three invariants, as defined in Eqs. (6)–(8), have derivatives of

$$\frac{\partial I_1}{\partial\mathbf{Q}} = \boldsymbol{\delta}\quad \frac{\partial I_2}{\partial\mathbf{Q}} = \boldsymbol{\delta}I_1 - \mathbf{Q}^{\mathrm{T}}\quad \frac{\partial I_3}{\partial\mathbf{Q}} = I_3\mathbf{Q}^{-\mathrm{T}} \tag{A4}$$

where $\boldsymbol{\delta}$ is the unit tensor.

If $\mathbf{a}$ and $\mathbf{b}$ are arbitrary vectors, the bilinear forms $\mathbf{a}\cdot\mathbf{Q}\cdot\mathbf{b}$ and $\mathbf{a}\cdot\mathbf{Q}^2\cdot\mathbf{b}$ have derivatives

$$\frac{\partial}{\partial\mathbf{Q}}(\mathbf{a}\cdot\mathbf{Q}\cdot\mathbf{b}) = \mathbf{ab} \tag{A5}$$

$$\frac{\partial}{\partial\mathbf{Q}^{\mathrm{T}}}(\mathbf{a}\cdot\mathbf{Q}^2\cdot\mathbf{b}) = \mathbf{ba}\cdot\mathbf{Q} + \mathbf{Q}\cdot\mathbf{ba} \tag{A6}$$

Appendix B. Derivatives of the stress

B.1. Interpolation of displacement

Using Eq. (43), displacement at any arbitrary point inside an element is interpolated as

$${}^{t+\Delta t}x_i^{(p)} = \sum_{k=1}^{n_{\mathrm{nie}}} h^k X_i^k + \sum_{k=1}^{n_{\mathrm{nie}}} h^k\ {}^{t+\Delta t}\lambda^{k,(p)}\ {}^{t+\Delta t}s_i^k \tag{B1}$$

where h^k is the interpolating function and n_{nie} is the number of nodes in an element. On differentiating this expression with respect to the reference material coordinate ${}^0\mathbf{x}$, we obtain the following expression for the displacement gradient tensor as a function of spine parameters,

$${}^{t+\Delta t}_{0}F_{ij}^{(p)} = \sum_{k=1}^{n_{\mathrm{nie}}} \frac{\partial h^k}{\partial {}^0x_j} X_i^k + \sum_{k=1}^{n_{\mathrm{nie}}} \frac{\partial h^k}{\partial {}^0x_j}\ {}^{t+\Delta t}\lambda^{k,(p)}\ {}^{t+\Delta t}s_i^k \tag{B2}$$

B.2. Differentiating the constitute equation

Using the notation of the finite element equations, the constitutive Eq. (36) for stress is written as

$${}^{t+\Delta t}T_{ij}^{(p)} = \frac{{}^{t+\Delta t}_{0}\kappa^{(p)}}{\det({}_0^{t+\Delta t}\mathbf{F}^{(p)})}\left[\frac{\partial W}{\partial\kappa}\right]^{(p)}{}^{t+\Delta t}n_i^{(p)}\ {}^{t+\Delta t}n_j^{(p)} \tag{B3}$$

The measure of compressive strain is

$${}^{t+\Delta t}_{0}\kappa^{(p)} = \frac{1}{\sqrt{{}^0\mathbf{n}\cdot[{}^{t+\Delta t}_{0}\mathbf{F}^{(p)}]^{-1}\cdot[{}^{t+\Delta t}_{0}\mathbf{F}^{(p)}]^{-\mathrm{T}}\cdot{}^0\mathbf{n}}} \tag{B4}$$

In the finite element formulation, the independent variables are the nodal degrees of freedom, ${}^{t+\Delta t}\lambda^{k,(p)}$. Stress ultimately depends on these variables, but for purposes of differentiation it is convenient to regard stress as a function of the following intermediate variables, which in turn depend on ${}^{t+\Delta t}\lambda^{k,(p)}$:

$${}^{t+\Delta t}T_{ij}^{(p)} = {}^{t+\Delta t}T_{ij}^{(p)}[{}^{t+\Delta t}_{0}\kappa^{(p)}, \det({}^{t+\Delta t}_{0}\mathbf{F}^{(p)}), {}^{t+\Delta t}n_i^{(p)}, {}^{t+\Delta t}n_j^{(p)}] \tag{B5}$$

We differentiate this expression using the chain rule:

$$\begin{aligned}\frac{\partial^{t+\Delta t}T_{ij}^{(p)}}{\partial^{t+\Delta t}\lambda^{k,(p)}} &= \frac{\partial^{t+\Delta t}T_{ij}^{(p)}}{\partial^{t+\Delta t}_{0}\kappa^{(p)}}\frac{\partial^{t+\Delta t}_{0}\kappa^{(p)}}{\partial^{t+\Delta t}\lambda^{k,(p)}} + \frac{\partial^{t+\Delta t}T_{ij}^{(p)}}{\partial^{t+\Delta t}n_i^{(p)}}\frac{\partial^{t+\Delta t}n_i^{(p)}}{\partial^{t+\Delta t}\lambda^{k,(p)}}\\ &+ \frac{\partial^{t+\Delta t}T_{ij}^{(p)}}{\partial^{t+\Delta t}n_j^{(p)}}\frac{\partial^{t+\Delta t}n_j^{(p)}}{\partial^{t+\Delta t}\lambda^{k,(p)}}\\ &+ \frac{\partial^{t+\Delta t}T_{ij}^{(p)}}{\partial\ \det({}^{t+\Delta t}_{0}\mathbf{F}^{(p)})}\frac{\partial\ \det({}^{t+\Delta t}_{0}\mathbf{F}^{(p)})}{\partial^{t+\Delta t}\lambda^{k,(p)}}\end{aligned} \tag{B6}$$

Using Eq. (B3), the derivatives of stress in Eq. (B6) can be computed as

$$\frac{\partial^{t+\Delta t}T_{ij}^{(p)}}{\partial_0{}^{t+\Delta t}\kappa^{(p)}} = \left(\frac{\partial W}{\partial\kappa} + \kappa\frac{\partial^2 W}{\partial\kappa^2}\right)^{(p)}\frac{{}^{t+\Delta t}n_i^{(p)}\ {}^{t+\Delta t}n_j^{(p)}}{\det({}^{t+\Delta t}_{0}\mathbf{F}^{(p)})} \tag{B7}$$

$$\frac{\partial^{t+\Delta t}T_{ij}^{(p)}}{\partial^{t+\Delta t}n_i^{(p)}} = \left(\kappa\frac{\partial W}{\partial\kappa}\right)^{(p)}\frac{{}^{t+\Delta t}n_j^{(p)}}{\det({}^{t+\Delta t}_{0}\mathbf{F}^{(p)})} \tag{B8}$$

$$\frac{\partial^{t+\Delta t}T_{ij}^{(p)}}{\partial\ \det({}^{t+\Delta t}_{0}\mathbf{F}^{(p)})} = -\left(\kappa\frac{\partial W}{\partial\kappa}\right)^{(p)}\frac{{}^{t+\Delta t}n_i^{(p)}\ {}^{t+\Delta t}n_j^{(p)}}{[\det({}^{t+\Delta t}_{0}\mathbf{F}^{(p)})]^2} \tag{B9}$$

The remaining terms in Eq. (B6) are calculated in the following sections.

B.3. Computing $(\partial\,{}^{t+\Delta t}_{0}\kappa^{(p)})/(\partial^{t+\Delta t}\lambda^{k,(p)})$

Using Eq. (B4), we can write the derivative of κ as

$$\frac{\partial\,{}^{t+\Delta t}_{0}\kappa^{(p)}}{\partial^{t+\Delta t}\lambda^{k,(p)}} = -\frac{1}{2F^{3/2}}\frac{\partial F}{\partial^{t+\Delta t}\lambda^{k,(p)}} \tag{B10}$$

where

$$F = [{}^{t+\Delta t}_{0}\kappa^{(p)}]^{-2} = {}^0\mathbf{n}\cdot[{}^{t+\Delta t}_{0}\mathbf{F}^{(p)}]^{-1}\cdot[{}^{t+\Delta t}_{0}\mathbf{F}^{(p)}]^{-\mathrm{T}}\cdot{}^0\mathbf{n} \tag{B11}$$

Since ${}^0\mathbf{n}$ is independent of deformation, the derivative of

F is

$$\frac{\partial F}{\partial {}^{t+\Delta t}\lambda^{k,(p)}} = {}^{0}\mathbf{n}\cdot\frac{\partial[{}^{t+\Delta t}_{0}\mathbf{F}^{(p)}]^{-1}}{\partial {}^{t+\Delta t}\lambda^{k,(p)}}\cdot[{}^{t+\Delta t}_{0}\mathbf{F}^{(p)}]^{-\mathrm{T}}\cdot{}^{0}\mathbf{n} + {}^{0}\mathbf{n}\cdot[{}^{t+\Delta t}_{0}\mathbf{F}^{(p)}]^{-1}\cdot\frac{\partial[{}^{t+\Delta t}_{0}\mathbf{F}^{(p)}]^{-\mathrm{T}}}{\partial {}^{t+\Delta t}\lambda^{k,(p)}}\cdot{}^{0}\mathbf{n} \quad \text{(B12)}$$

The derivatives on the right-hand side of this equation are computed as:

$$\frac{\partial[{}^{t+\Delta t}_{0}\mathbf{F}^{(p)}]^{-1}}{\partial {}^{t+\Delta t}\lambda^{k,(p)}} = -[{}^{t+\Delta t}_{0}\mathbf{F}^{(p)}]^{-1}\cdot\frac{\partial {}^{t+\Delta t}_{0}\mathbf{F}^{(p)}}{\partial {}^{t+\Delta t}\lambda^{k,(p)}}\cdot[{}^{t+\Delta t}_{0}\mathbf{F}^{(p)}]^{-1} \quad \text{(B13)}$$

where, from Eq. (B2), we get

$$\frac{\partial {}^{t+\Delta t}_{0}\mathbf{F}^{(p)}}{\partial {}^{t+\Delta t}\lambda^{k,(p)}} = \frac{\partial h^{k}}{\partial {}^{0}x_{j}}\,{}^{t+\Delta t}s_{i}^{k} \quad \text{(B14)}$$

Once the derivative of the inverse of ${}_{0}{}^{t+\Delta t}\mathbf{F}^{(p)}$ is known, the derivative of its transpose is simply the transpose of the derivative.

B.4. Computing $(\partial {}^{t+\Delta t}n_{i}^{(p)})/(\partial {}^{t+\Delta t}\lambda^{k,(p)})$

The upper and lower surfaces of each 3D element form part of the fiber mat interfaces in the preform stack [15], and these interfaces are material surfaces. We find the unit normal vector ${}^{t+\Delta t}n_{i}^{(p)}$ by computing a material normal vector ${}^{t+\Delta t}\mathcal{N}_{i}^{(p)}$ at the desired point and then normalizing it to unit length. At any point inside the element this vector is interpolated from nodal values ${}^{t+\Delta t}\mathbf{N}^{k,(p)}$ as follows:

$${}^{t+\Delta t}\mathcal{N}_{i}^{(p)} = \sum_{k=1}^{n_{nie}} h^{k}\frac{{}^{t+\Delta t}N_{i}^{k,(p)}}{\|{}^{t+\Delta t}\mathbf{N}^{k,(p)}\|} \quad \text{(B15)}$$

The upper and lower faces of each brick element can be treated as isoparametric quadrilateral elements, from which the material normals corresponding to the top and bottom surfaces are computed using

$${}^{t+\Delta t}\mathbf{N}^{k,(p)} = \mathbf{Z}\times\mathbf{E} \quad \text{(B16)}$$

where

$$\mathbf{Z} = \sum_{l=1}^{4}\frac{\partial g_{l}}{\partial\xi}\,{}^{t+\Delta t}\mathbf{x}^{l,(p)} \qquad \mathbf{E} = \sum_{l=1}^{4}\frac{\partial g_{l}}{\partial\eta}\,{}^{t+\Delta t}\mathbf{x}^{l,(p)} \quad \text{(B17)}$$

In these expressions g_l represents the two-dimensional shape functions corresponding to node l for the upper or lower quadrilateral element, and ξ and η are the element coordinates.

Differentiating ${}^{t+\Delta t}n_{i}^{(p)}$ with respect to the spine parameter ${}^{t+\Delta t}\lambda^{k,(p)}$ involves computing the derivative of $\mathbf{Z}$, which is obtained from

$$\frac{\partial\mathbf{Z}}{\partial {}^{t+\Delta t}\lambda^{k,(p)}} = \left.\frac{\partial g}{\partial\xi}\right|_{\xi^{k},\eta^{k}}{}^{t+\Delta t}\mathbf{s}^{k} \quad \text{(B18)}$$

with k being the node where the derivative is being evaluated. $\partial\mathbf{E}/(\partial {}^{t+\Delta t}\lambda^{k,(p)})$ is derived similarly.

Now using Eqs. (B15)–(B18), $(\partial {}^{t+\Delta t}n_{i}^{(p)})/(\partial {}^{t+\Delta t}\lambda^{k,(p)})$ can be computed. Some simplification in Eq. (B17) results for the wedge elements, because the upper and lower triangular faces of the element are planar.

B.5. Computing $(\partial\,\det({}^{t+\Delta t}_{0}\mathbf{F}^{(p)}))/(\partial {}^{t+\Delta t}\lambda^{k,(p)})$

Using the laws of tensor algebra, one can write

$$\frac{\partial\,\det({}^{t+\Delta t}_{0}\mathbf{F}^{(p)})}{\partial {}^{t+\Delta t}\lambda^{k,(p)}} = \det({}^{t+\Delta t}_{0}\mathbf{F}^{(p)})[{}^{t+\Delta t}_{0}\mathbf{F}^{(p)}]^{-\mathrm{T}} : \frac{\partial {}^{t+\Delta t}_{0}\mathbf{F}^{(p)}}{\partial {}^{t+\Delta t}\lambda^{k,(p)}} \quad \text{(B19)}$$

The right-hand side of this equation can be computed using Eqs. (B2) and (B14).

Appendix C. Derivatives of the incremental strain

The incremental strain ${}_{t+\Delta t}\epsilon_{ij}^{(p)}$ is defined in Eq. (48). On differentiating this with respect to the spine parameter, we get:

$$\frac{\partial_{t+\Delta t}\epsilon_{ij}^{(p)}}{\partial {}^{t+\Delta t}\lambda^{l,(p)}} = \frac{1}{2}\left(\frac{\partial_{t+\Delta t}u_{i,j}^{(p)}}{\partial {}^{t+\Delta t}\lambda^{l,(p)}} + \frac{\partial_{t+\Delta t}u_{j,i}^{(p)}}{\partial {}^{t+\Delta t}\lambda^{l,(p)}} + {}_{t+\Delta t}u_{k,i}^{(p)}\frac{\partial_{t+\Delta t}u_{k,j}^{(p)}}{\partial {}^{t+\Delta t}\lambda^{l,(p)}} + \frac{\partial_{t+\Delta t}u_{k,i}^{(p)}}{\partial {}^{t+\Delta t}\lambda^{l,(p)}}\,{}_{t+\Delta t}u_{k,j}^{(p)}\right) \quad \text{(C1)}$$

where a comma in a right subscript denotes partial differentiation with respect to the coordinates indicated by the left subscript, i.e.

$${}_{t+\Delta t}u_{i,j}^{(p)} = \frac{\partial u_{i}^{(p)}}{\partial {}^{t+\Delta t}x_{j}^{(p)}} \quad \text{(C2)}$$

From Eqs. (48), (49) and (B1), one obtains the following expression,

$${}_{t+\Delta t}u_{i,j}^{(p)} = \sum_{k=1}^{n_{\mathrm{nie}}}\frac{\partial h^{k}}{\partial {}^{t+\Delta t}x_{j}^{(p)}}({}^{t+\Delta t}s_{i}^{k}\,{}^{t+\Delta t}\lambda^{k,(p)} - {}^{t}s_{i}^{k}\,{}^{t}\lambda^{k}) \quad \text{(C3)}$$

On differentiating this with respect to ${}^{t+\Delta t}\lambda^{l,(p)}$, we get:

$$\frac{\partial_{t+\Delta t}u_{i,j}^{(p)}}{\partial {}^{t+\Delta t}\lambda^{l,(p)}} = \frac{\partial h^{l}}{\partial {}^{t+\Delta t}x_{j}^{(p)}}\,{}^{t+\Delta t}s_{i}^{l} \quad \text{(C4)}$$

Then, substituting Eqs. (C2) and (C3) into Eq. (C1) and

simplifying, we get

$$\frac{\partial_{t+\Delta t}\epsilon_{ij}^{(p)}}{\partial^{t+\Delta t}\lambda^{l,(p)}} = \frac{1}{2}\Bigg[\frac{\partial h^l}{\partial^{t+\Delta t}x_j^{(p)}}\,{}^{t+\Delta t}s_i^l + \frac{\partial h^l}{\partial^{t+\Delta t}x_i^{(p)}}\,{}^{t+\Delta t}s_j^l + \frac{\partial h^l}{\partial^{t+\Delta t}x_j^{(p)}} \times\Bigg(\sum_{k=1}^{n_{\text{nie}}}\frac{\partial h^k}{\partial^{t+\Delta t}x_i^{(p)}}({}^{t+\Delta t}\mathbf{s}^k.{}^{t+\Delta t}\mathbf{s}^l\,{}^{t+\Delta t}\lambda^{k,(p)} - {}^{t}\mathbf{s}^k.{}^{t+\Delta t}\mathbf{s}^l\,{}^{t}\lambda^k)\Bigg) + \frac{\partial h^l}{\partial^{t+\Delta t}x_i^{(p)}}\Bigg(\sum_{k=1}^{n_{\text{nie}}}\frac{\partial h^k}{\partial^{t+\Delta t}x_j^{(p)}}({}^{t+\Delta t}\mathbf{s}^k.{}^{t+\Delta t}\mathbf{s}^l\,{}^{t+\Delta t}\lambda^{k,(p)} - {}^{t}\mathbf{s}^k.{}^{t+\Delta t}\mathbf{s}^l\,{}^{t}\lambda^k)\Bigg)\Bigg] \tag{C5}$$

On differentiating Eq. (C3) further with respect to ${}^{t+\Delta t}\lambda^{l,(p)}$, it is easy to show that $(\partial^2({}_{t+\Delta t}u_{i,j}^{(p)}))/(\partial({}^{t+\Delta t}\lambda^{l,(p)})^2)$, and all other similar double derivatives appearing due to further differentiation of Eq. (C1), are identically zero. As a result, differentiation of Eq. (C1) yields:

$$\frac{\partial^2{}_{t+\Delta t}\epsilon_{ij}^{(p)}}{\partial^{t+\Delta t}\lambda^{m,(p)}\,\partial^{t+\Delta t}\lambda^{l,(p)}} = \frac{1}{2}\left(\frac{\partial_{t+\Delta t}u_{k,i}^{(p)}}{\partial^{t+\Delta t}\lambda^{m,(p)}}\frac{\partial_{t+\Delta t}u_{k,j}^{(p)}}{\partial^{t+\Delta t}\lambda^{l,(p)}} + \frac{\partial_{t+\Delta t}u_{k,i}^{(p)}}{\partial^{t+\Delta t}\lambda^{l,(p)}}\frac{\partial_{t+\Delta t}u_{k,j}^{(p)}}{\partial^{t+\Delta t}\lambda^{m,(p)}}\right) \tag{C6}$$

We substitute Eq. (C3) in the above equation and simplify to obtain the following

$$\frac{\partial^2{}_{t+\Delta t}\epsilon_{ij}^{(p)}}{\partial^{t+\Delta t}\lambda^{m,(p)}\,\partial^{t+\Delta t}\lambda^{l,(p)}} = \frac{1}{2}\left(\frac{\partial h^o}{\partial^{t+\Delta t}x_i^{(p)}}\frac{\partial h^l}{\partial^{t+\Delta t}x_j^{(p)}} + \frac{\partial h^l}{\partial^{t+\Delta t}x_i^{(p)}}\frac{\partial h^o}{\partial^{t+\Delta t}x_j^{(p)}}\right){}^{t+\Delta t}\mathbf{s}^l.{}^{t+\Delta t}\mathbf{s}^o \tag{C7}$$

References

[1] Fracchia CA, Castro J, Tucker III CL. A finite element/control volume simulation of resin transfer molding. Proceedings of the American Society for Composites Fourth Technical Conference, Lancaster, PA: Technomic, 1989. p. 157–66.

[2] Molnar J, Trevino L, Lee LJ. Liquid flow in molds with prelocated fiber mats. Polym Compos 1989;10:414–23.

[3] Bruschke MV, Advani SG. A finite element/control volume approach to mold filling in anisotropic porous media. Polym Compos 1990;11:398–405.

[4] Bruschke MV, Advani SG. RTM filling simulation of complex three dimensional shell-like structures. SAMPE Q 1991;23(1):2–11.

[5] Young WB, Rupel K, Han K, Lee LJ, Liou MJ. Analysis of resin injection molding in molds with preplaced fiber mats. II: Numerical simulation and experiments of mold filling. Polym Compos 1991;12:30–8.

[6] Young WB, Han K, Fong LH, Lee LJ, Liou MJ. Flow simulation in molds with preplaced fiber mats. Polym Compos 1991;12:391–403.

[7] Tucker III CL, Dessenberger RB. Governing equations for flow and heat transfer in stationary fiber beds. In: Advani SG, editor. Flow and rheolgy in polymer composites manufacturing, Amsterdam: Elsevier, 1994. p. 257–323.

[8] Advani SG, Bruschke MV, Parnas RS. Resin transfer molding flow phenomena in polymeric composites. In: Advani SG, editor. Flow and rheolgy in polymer composites manufacturing, Amsterdam: Elsevier, 1994. p. 465–515.

[9] Han K, Trevino L, Lee LJ, Liou M. Polym Compos 1993;14(2):144–50.

[10] Lekakou C, Johari MAKB, Bader MG. Compressibility and flow permeability of two-dimensional woven reinforcements in the processing of composites. Polym Compos 1996;17:666–72.

[11] Luce TL, Advani SG, Grant Howard J, Parnas RS. Permeability characterization. Part 2: Flow behavior in multiple-layer preform. Polym Compos 1995;16:446–58.

[12] Pearce N, Summerscales J. The compressibility of a reinforcement fabric. Compos Manufacturing 1995:6.

[13] Phelan Jr. FR. Simulation of the injection process in resin transfer molding. Polym Compos 1997;18(4):460–76.

[14] Phelan Jr. FR. Analysis of injection/compression liquid composite molding process variants. ASME Proceedings, 1996. Presented at the 1996 ASME International Mechanical Engineering Congress and Exhibition, Atlanta, GA.

[15] Pillai KM, Tucker III CL, Phelan Jr. FR. Numerical simulation of injection/compression liquid composite molding. Part 1: Mesh generation. Composites Part A 2000;31:87–94.

[16] Phelan Jr. FR, Pillai KM, Tucker III CL. Numerical simulation of injection/compression liquid composite molding. Part 3: Mold filling, in preparation.

[17] Fanucci JP, Nolet S, McCarthy S. Pultrusion of composites. In: Gutowski TG, editor. Advanced composites manufacturing, New York: Wiley, 1997. p. 259–95.

[18] Green AE, Adkins JE. Large elastic deformations. Oxford: Oxford University Press, 1960.

[19] Treloar LRG. The physics of rubber elasticity. 3rd ed.. Oxford: Clarendon Press, 1975.

[20] Lurie AI. Nonlinear theory of elasticity. Amsterdam: Elsevier, 1990.

[21] Gutowski TG, Dillon G. The elastic deformation of fiber bundles. In: Gutowski TG, editor. Advanced composites manufacturing, New York: Wiley, 1997. p. 115–56.

[22] Bathe KJ. Finite element procedures. Englewood Cliffs, NJ: Prentice Hall, 1996.